Design and Evaluation of a Novel Efficient Air-Assisted Hollow-Cone Electrostatic Nozzle

Li Zhang , Zhi Li , Huaxing Chu , Qiaolin Chen , Yang Li * , Xinghua Liu *

Posted Date: 16 May 2025

doi: 10.20944/preprints202505.1301.v1

Keywords: electrostatic spraying; hollow-cone nozzle; conductive liquid film; parameter optimization; charge-to-mass ratio

 doi:10.20944/preprints202505.1301.v1

Article

Design and Evaluation of a Novel Efficient Air-Assisted Hollow-Cone Electrostatic Nozzle

Li Zhang [1], Zhi Li [2], Huaxing Chu [2], Qiaolin Chen [2], Yang Li [2,3,*] and Xinghua Liu [2,3,*]

[1] College of Resources, Shandong University of Science and Technology, Tai'an 271019, China
[2] College of Mechanical & Electronic Engineering, Shandong Agricultural University, Tai'an 271018, China
[3] Shandong Key Laboratory of Intelligent Production Technology and Equipment for Facility Horticulture, Tai'an 271018, China
* Correspondence: mtlyab@sdau.edu.cn (Y.L.); lxh9357@163.com (X.L.).

Abstract: For crop protection, electrostatic spraying technology significantly improves deposition uniformity and pesticide utilization through the "wraparound -adsorption" effect of charged droplets. However, existing hydraulic atomization electrostatic nozzles suffers from low charge-to-mass ratios due to unclear optimization principles for electrode parameters. To this end, this study designs and evaluates a novel air-assisted hydraulic-atomization hollow-cone electrostatic nozzle. First, the air-assisted hollow-cone nozzle was designed. Then, high-speed imaging was employed to obtain liquid film morphological parameters (length: 2.14 mm, width: 1.96 mm, spray angle: 49.25°). Based on these parameters, an electric field simulation model of the electrostatic nozzle was established to analyze the influence of electrode parameters on charging performance and identify the optimal parameter combination. Finally, evaluation experiments were conducted for the feasibility and efficiency of the designed electrostatic nozzle. The experimental results demonstrate that electrode cross-sectional dimensions exhibit a positive correlation with surface charge density of pesticide liquid film. Besides, optimal charging performance will be obtained when the electrode plane coincides with the tangent plane of the liquid film leading edge. Based on these charging laws, the optimal electrode parameters were determined as: 2.0×2.0 mm cross-section with a 3.8 mm distance from nozzle tip to the electrode. With the optimized parameters, the nozzle achieved a droplet charge-to-mass ratio of 4.9 mC/kg under the charging voltage of 3.0 kV. The charged droplets achieved deposition coverages of 12.19%, 5.72%, and 5.91% on abaxial leaf surfaces in the upper, middle, and lower soybean canopy respectively, which is a significant improvement in deposition uniformity. This study provides helpful theoretical guidance and technical references for electrostatic nozzle design and application.

Keywords: electrostatic spraying; hollow-cone nozzle; conductive liquid film; parameter optimization; charge-to-mass ratio

1. Introduction

For non-electrostatic pesticide spraying application, pesticide droplets often fail to penetrate crop canopies and reach abaxial leaf surfaces. Furthermore, leaf inclination angles and surface characteristics - particularly those with thick cuticular wax layers or dense trichomes - frequently lead to droplet loss during spraying application. To address these challenges, induction-charging electrostatic nozzles are utilized to electrically charge pesticide droplets through electrostatic induction principles. The charged droplets demonstrate significantly enhanced deposition on crop foliage through the " wraparound -adsorption" effect. Thereby electrostaic spraying improves pesticide utilization while reducing environmental contamination [1–4]. When charged droplets penetrate deep into target crop canopies, their movement against gravitational forces is driven by the electric field force. Then, the charge-to-mass ratio (Q/M) is a critical parameter determining deposition efficacy [5–8]. Consequently, enhancing the initial charge-to-mass ratio at the nozzle exit

 doi:10.20944/preprints202505.1301.v1

- fundamentally determined by the charge density of the pesticide liquid film in the electrified atomization zone - represents the core approach for optimizing droplet charging performance.

According to Gauss's theorem, the spatial electric field distribution within the charging-atomization zone of electrostatic nozzles is the critical factor determining the charge density of the liquid film. Relative researches demonstrate that electrode parameters significantly influence both the electric field in the charging-atomization zone and the charge-to-mass ratio. Patel et al. [9] systematically investigated the effects of electrode material, geometric dimensions, and spatial positioning on charging performance, revealing that an electrode-to-nozzle distance of 2.0-3.0 mm yields an optimal charge-to-mass ratio of 2.8 mC/kg. Mamidi V.R. [10] and Laryea G.N.[11] achieved droplet charge-to-mass ratios of 0.27 mC/kg and 0.42 mC/kg respectively through optimal designs of the internal charging structures of the hydraulic electrostatic nozzles. J.Wang et al.[12] established a theoretical formula for droplet swarm charge quantity, examined the influence of charging electrode diameter, charging voltage, and atomization pressure on charging performance, and achieved the droplet charge-to-mass ratio of approximately 0.30 mC/kg. Jinlong Lin et al. [13] enhanced the maximum droplet charge-to-mass ratio to 4.4 mC/kg (an 84% improvement over pre-optimization performance) by implementing waist-shaped electrodes in fan-type electrostatic nozzles. Brentjes et al. [14] developed an electric field distribution model for the charging zone and predicted spray droplet charge levels. Additional studies indicate that charged droplet clouds within the atomization zone also affect charging efficiency. S. Zhao et al.[15] revealed the influence of space charge during the charging process. Kacprzyk [16] employed high-speed imaging technology to observe pneumatic atomization processes, revealing the shielding effect of umbrella-shaped atomized liquid on the electric field of columnar liquid charging. These research outcomes provide meaningful theoretical foundations for the structural design and optimization of the electrostatic nozzle.

In the field of pesticide spraying for crop protection, hydraulic atomization hollow cone nozzles have gained widespread application due to their superior atomization characteristics, including uniform droplet size distribution, high coverage rate, and excellent compatibility. Its atomization process contains three consecutive stages: First, the liquid is ejected from the nozzle under hydraulic pressure to form a continuous liquid film. Subsequently, the liquid film develops to form undulations and perforations under initial disturbances. Finally, the liquid film ruptures at these perforations to form liquid filaments, which further break up into discrete droplets [17]. Notably, since pesticide solutions contain abundant ions, the structural characteristics of the conductive liquid films significantly influence spatial electric field distribution [18,19]. The interaction between the charged liquid film and the surrounding electric field plays a crucial role in determining droplet charging efficiency.

Regrettably, current research exhibits significant limitations: although experimental methods have been used to optimize electrode parameters for specific nozzle configurations, a universal theoretical framework for electrode optimization has yet to be established. Moreover, these studies have generally neglected the influence of the conductive liquid film on the electric field distribution, resulting in substantial discrepancies between theoretical models and actual electric field. This crucial oversight not only severely compromises the optimization accuracy of the electrostatic nozzle but also directly causes the prevalent issue of low charging efficiency in hydraulic atomization nozzles.

To address these issues, this study employs numerical simulation and actual experiment to investigate the influence mechanisms of electrode parameters on droplet charging characteristics, and optimally designs a novel efficient hollow-cone electrostatic nozzle. The research methodology comprises three key phases: First, an air-assisted hollow-cone nozzle was designed. Then, high-speed imaging technology was utilized to quantitatively characterize the dynamic behavior of liquid films from hollow-cone nozzles, obtaining critical parameters to describe liquid film morphology evolution. Subsequently, based on the parameters, a three-dimensional electric field model of the electrostatic nozzle was developed to elucidate the regulatory effects of electrode spatial location and geometric dimensions on electric field distribution and liquid film charge density. This model enabled parameter optimization to determine the optimal electrode configuration. Finally, systematic

 doi:10.20944/preprints202505.1301.v1

experiments were conducted to validate the influence of electrode parameters on droplet charging performance, and the deposition efficacy of the optimized electrostatic nozzles on target crop.

2. Materials and Methods

2.1. Structure Design of Nozzle Body

This study developed a novel concentric two-phase flow air-assisted hollow-cone electrostatic nozzle (Figure 1), whose working principle is as follows: The liquid medium is transported through the liquid flow channel to a hollow-cone nozzle (1/8-FD1-ss, BYCO), where it forms a swirling flow in the vortex chamber before being ejected from the nozzle outlet to create a hollow-cone liquid film. The nozzle employs air-assisted technology to enhance atomization performance. Specifically, compressed gas enters the nozzle body through the gas flow channel and sequentially passes through the vortex chamber and flow-focusing chamber and finally enters into the charging-atomization zone. Then, the gas interacts with the liquid film, which optimizes atomization performance while preventing electrode wetting [20]. This design not only significantly improves atomization effectiveness but also effectively controls droplet trajectories through airflow confinement, thereby improving the droplet penetration capability within the crop canopy.

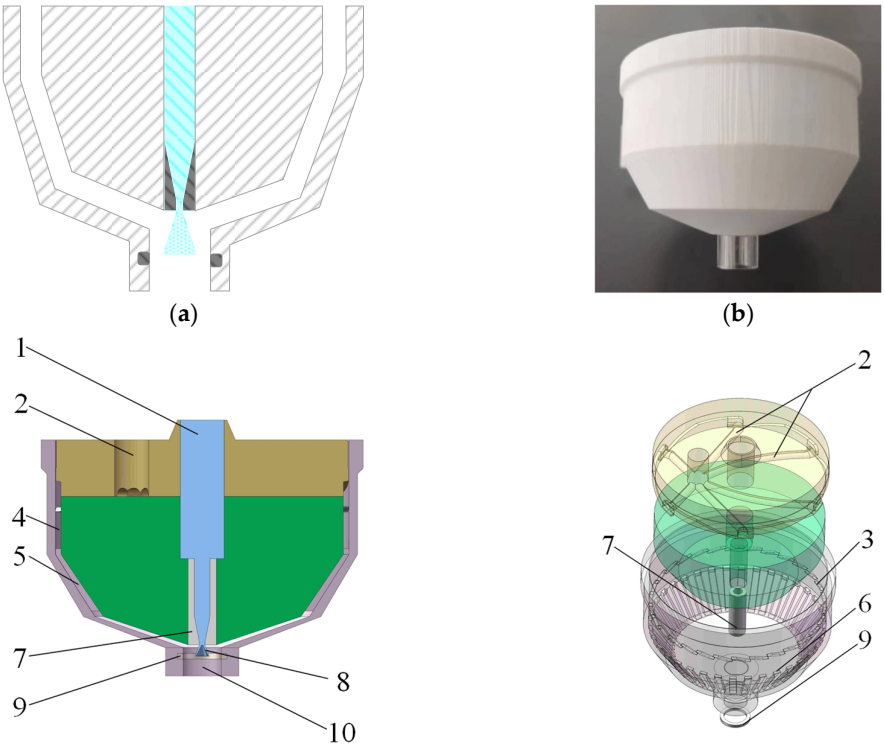

1 Liquid medium flow channel; 2 Gas medium flow channel; 3 Swirl plate; 4 Swirl chamber; 5 Constriction plate; 6 Constriction chamber; 7 Metal nozzle; 8 Hollow-cone liquid film; 9 Annular electrode; 10 Charged atomization zone.

(c)

Figure 1. Nozzle body structure diagram: (a) Cross-sectional view of nozzle body; (b) Physical photograph of nozzle body; (c) Exploded view of nozzle body structure.

During hydraulic atomization process, the pesticide liquid is injected into the air medium as a high-speed jet. The significant slip velocity and density gradient between the liquid and gas phase induce strong instability at the liquid film surface. This hydrodynamic instability promotes liquid film disintegration, forming elongated ligament structures that ultimately break up into discrete droplets [21]. During normal operation of electrostatic nozzles, the charging-atomization zone

 doi:10.20944/preprints202505.1301.v1

exhibits multiphysics coupling involving simultaneous interactions between liquid medium, gas medium, and electric field. Relative research demonstrates that assisted airflow not only modifies liquid film morphology but also influences its breakup patterns and atomization performance [22,23].

2.2. Liquid Film Morphology Based on High-Speed Imaging

This study employed a high-speed imaging system (Phantom EVO410L, Vision Research) to quantitatively characterize the dynamic behavior of liquid films, systematically investigating liquid film evolution under the comprehensive effect of hydraulic and pneumatic atomization. As shown in Figure 2, the experimental setup comprises three subsystems: (1) Hydraulic supply system: A plunger pump (BH320, Himore) provided stable water pressure at 2 MPa, with precise pressure control achieved through a control console and regulating valve; (2) Air-assist system: An air compressor (OTS-1500W-40L, OutStanding) generated an airflow with a constant velocity of 50 m/s; (3) Image acquisition system: A high-speed camera was configured for real-time recording of liquid film breakup process. To ensure the optical observation quality, the experiments specifically utilized transparent acrylic tubing as the nozzle housing material. During the liquid atomization experiment, the liquid first underwent primary atomization at the hollow-cone nozzle under hydraulic pressure, followed by secondary pneumatic atomization through airflow-liquid interaction. Detailed parameter configurations for the high-speed imaging system are provided in Table 1.

Table 1. Parameter configurations of high-speed imaging system.

Main Parameters	Value
Frame rate	20000 fps
Exposure time	20 μs
Pixel size	512×256
Shooting elevation angle	27.5 °

As illustrated in Figure 3, this study categorizes the liquid atomization process into three characteristic regions: the liquid film region, the ligament region, and the droplet region [24]. To obtain the dimensional parameters of the liquid film, the distance between the nozzle orifice and the rupture position of the liquid film leading edge is defined as the liquid film length L, the width of the ruptured leading edge as D, and the atomization angle as α. During liquid atomization, the pesticide liquid first forms ligament structures. It should be noted that once these ligaments separate from the main liquid film body, the charge conduction path is immediately interrupted, resulting in the stabilization of their carried charge quantity. These detached ligaments undergo further breakup under aerodynamic disturbances, ultimately forming discrete pesticide droplets. Consequently, the charge density at the leading edge of the liquid film becomes the determining factor for the ultimate droplet charge-to-mass ratio.

 doi:10.20944/preprints202505.1301.v1

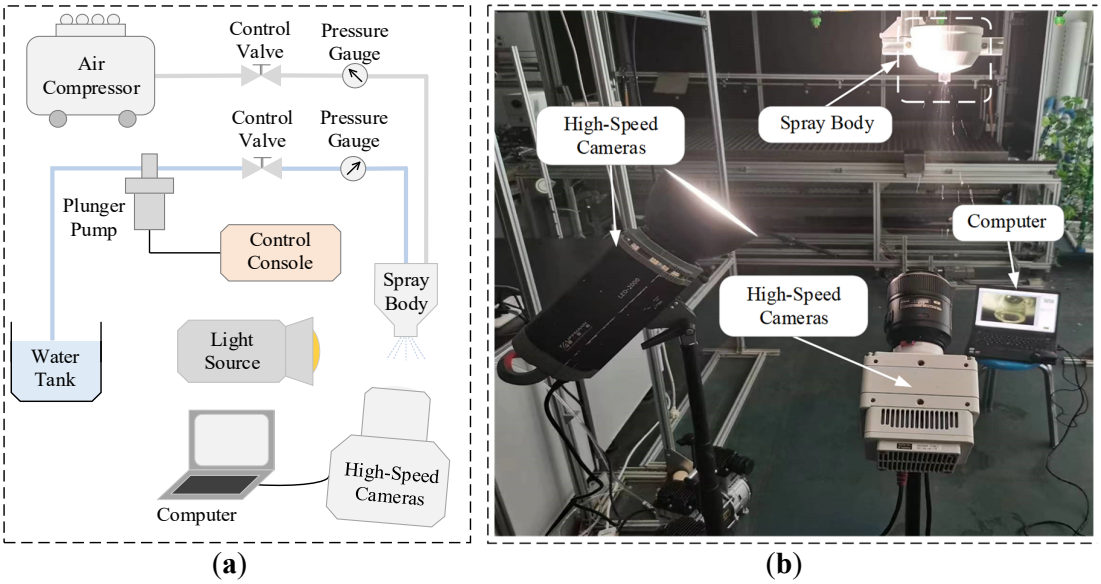

Figure 2. High-Speed Imaging Platform: (a) Schematic diagram of the high-speed imaging platform setup; (b) Physical photograph of the high-speed imaging platform.

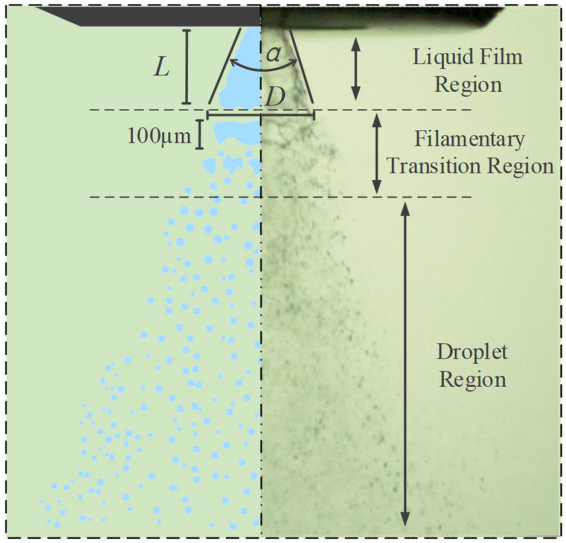

Figure 3. Schematic diagram of the liquid film breakup and atomization process.

2.3. Electrostatic Field Modeling of the Electrostatic Nozzle

Under the influence of the electrostatic field, free charges within the liquid medium undergo directional migration and redistribute themselves on the liquid film surface. The surface charge distribution, influenced by the liquid film's morphological characteristics, consequently affects the electric field distribution in the charging zone. When the surface charge density remains below the Rayleigh limit [25], its magnitude primarily depends on the local electric field strength. An increase in field strength directly enhances the surface charge density. As the charge density progressively approaches the Rayleigh limit within the liquid, the electric field force overcomes surface tension, inducing the liquid film rupture. However, it is noteworthy that existing studies have demonstrated that in practical electrostatic atomization processes, the actual charge carried by droplets typically reaches only about 10% of the Rayleigh limit [26,27]. There is still a lot of improvement room for the droplet charge-to-mass ratio. And further investigation of spatial electric field distribution in the

 doi:10.20944/preprints202505.1301.v1

charging-atomization zone holds significant importance for better charging performance of the electrostatic nozzle.

To establish a numerical model of the electric field distribution in the charging-atomization zone, the charging electrode was connected to the positive polar of a DC-current power source, while the liquid medium ejected from the nozzle was connected to the negative polar and maintained at the ground potential. Excited by the charging voltage, the resulting charging electrostatic field within the nozzle body can be described by Equation (1). Under this electric field, the conductive liquid medium exhibits directional charge migration, quantitatively characterized by the current density in Equation (2). By simultaneously solving Equations (1) and (2), the charge continuity equation is obtained as shown in Equation (3). Furthermore, based on Gauss's law, the spatial charge density distribution at any position can be derived in Equation (4).

$$E = -\nabla\varphi, \tag{1}$$

$$J = \sigma E + J_e, \tag{2}$$

$$\nabla \cdot J = -\nabla \cdot (\sigma\nabla\varphi - J_e), \tag{3}$$

$$-\nabla \cdot (\varepsilon\nabla\varphi - P) = \rho \tag{4}$$

where ε represents the liquid medium's dielectric constant, P denotes the polarization vector, σ denotes medium conductivity and ρ indicates the spatial charge density.

To investigate the influence of electrode spatial position and dimensional parameters on the induced charge density at the liquid film surface, a systematic numerical simulation study was conducted. Based on the measured morphological parameters of the liquid film and nozzle structural characteristics, an electric field simulation model of the charging-atomization zone was established. Considering the axisymmetric feature of the hollow-cone nozzle, a simplified two-dimensional axisymmetric model was constructed to reduce computation load.

As shown in Figure 5, the parameter configuration of the charging electrode was established as follows: A Cartesian coordinate system was defined with its origin at the center of the nozzle orifice (X-Y axes orientation as illustrated). To prevent droplet-induced electrode wetting, the inner diameter of the annular charging electrode was fixed at 13 mm. Three critical geometric parameters were specified: (1) electrode installation height y (vertical distance from the electrode's lower surface to the X-axis); (2) electrode cross-sectional length l; and (3) electrode cross-sectional width d. The combination (l, d, y) completely characterizes the electrode's spatial configuration. Through systematic adjustment of these parameter configurations, the electric field distribution were obtained, thereby enabling the optimal parameter configuration of the charging electrode that maximizes surface charge density on the liquid film.

For boundary conditions: The metal hollow-cone nozzle was grounded to keep the earth potential. The annular charging electrode was set with a positive potential of 1 kV. Material parameters were specified as: the nozzle body constructed with the insulating nylon; the liquid medium is tap water (conductivity 0.0313 S/m, relative permittivity 81); and environmental conditions maintained at standard atmospheric state.

 doi:10.20944/preprints202505.1301.v1

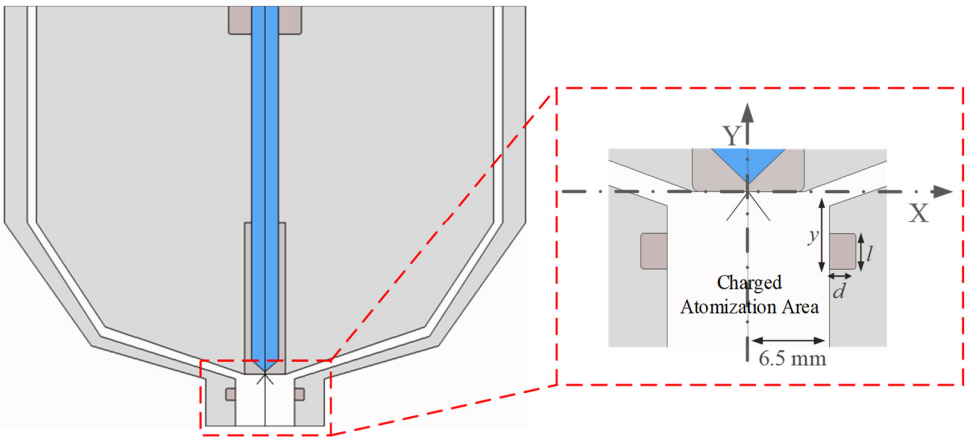

Figure 4. Simulation model of the hollow-cone electrostatic nozzle.

2.4. Design of Annular Electrode Based on Particle Swarm Optimization

Three key geometric parameters of the annular electrode were selected as optimization variables: spatial position parameter y and cross-sectional dimensions (l, d). The optimization ranges were set: cross-sectional length $l \in [1,5]$ mm, width $d \in [1,5]$ mm; spatial position $y \in [-12,2]$ mm. With the surface charge density at the liquid film leading edge as the optimization objective, systematic calculations of charge density distributions under different parameter combinations were performed to determine the optimal electrode parameter configuration.

Using parametric scanning methodology, simulation tests were conducted with a step size of 0.5 mm across the defined range, yielding a total of 2349 charge density data samples. The dataset was randomly partitioned into training and validation sets at ratios of 85% and 15%. Subsequently, a backpropagation (BP) neural network model incorporating 5 hidden layer nodes was constructed to establish a nonlinear fitting function for the simulation model. The trained BP neural network served as the objective function for the particle swarm optimization (PSO) algorithm, which performed global optimization searches within the parameter space through iterative updates of particle positions and velocity vectors. After multiple iterative computations, the optimal electrode parameter configuration with the maximum surface charge density was ultimately determined.

2.5. Charging Performance Verification of the Optimized Electrostatic Nozzle

To validate the effectiveness of the optimized electrostatic nozzle on droplet charging characteristics and application quality, this study designed and constructed a comprehensive pesticide application evaluation platform as in Figure 5. The platform was employed for quantitative analysis of two critical performance indicators: Firstly, precise measurement of droplet charge-to-mass ratio was conducted to verify the charging performance of the optimized electrostatic nozzle; secondly, measurements of foliar deposition coverage with the optimized electrostatic mode, the unoptimized electrostatic mode, and the conventional hydraulic-atomization mode without electrostatic charging were conducted to evaluate the spraying quality improvement of the optimized electrostatic nozzle. The integrated system enabled simultaneous assessment of both fundamental charging characteristics and practical application effects, providing a complete evaluation framework from basic electrode parameters to field spraying performance metrics.

As shown in Figure 5, the charge-to-mass ratio measurement platform primarily consists of three subsystems: a high-voltage power supply system, a charge collection system, and a liquid mass measurement system. The annular electrode is connected via an ammeter (15B MAX, Fluke) to a continuously adjustable DC high-voltage generator (2671-AM, ReK) capable of providing 0-10 kV output. The microampere-level leakage current monitored by the ammeter serves as an indirect indicator of the charging electric field performance in high-humidity atomization conditions. Additionally, a mesh-targeted collection device is positioned below the nozzle to capture charged

 doi:10.20944/preprints202505.1301.v1

droplets, with the collected charge flowing to the ground through a high-precision multimeter (DMM/6500, Keithley) for accurate measurement of the charging current per unit time. Beneath the mesh target, a droplet collection apparatus is installed to measure the liquid mass output during the same time interval. The droplet charge-to-mass ratio is then calculated according to the formula (5)

$$\lambda = \frac{Q}{M} = \frac{It}{M} \tag{5}$$

where λ represents the average charge-to-mass ratio of the charged droplet, I denotes the charging current measured by the high-precision multimeter, and M is the liquid mass collected over the same duration. By synchronously acquiring current and droplet mass data, the droplet charge-to-mass ratio can be calculated.

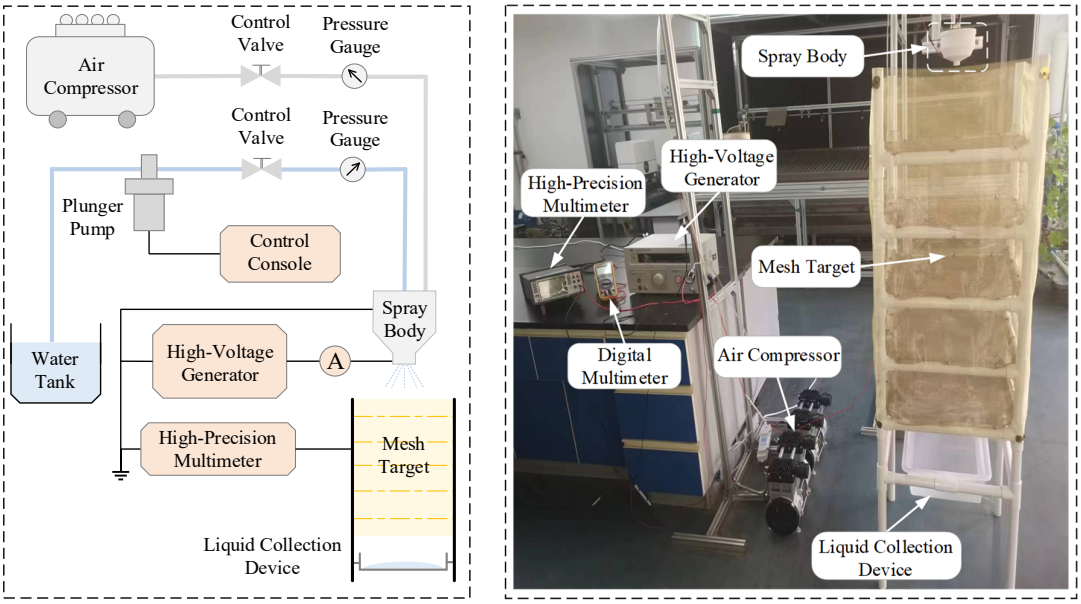

Figure 5. Charge-to-mass ratio measurement platform: (a) Schematic diagram of the measurement platform; (b) Physical photograph of the measurement platform.

The spray unit was mounted on a horizontal sliding rail via a pulley mechanism, with soybean plants positioned 1 m below the rail. To comprehensively analyze droplet deposition characteristics on soybean leaves, water-sensitive papers were deployed on both the adaxial and abaxial leaf surfaces at the upper, middle, and lower soybean canopy. During spraying experiments, the spray unit was driven horizontally along the rail at a constant speed of 1 m/s by an electric motor. Spraying performances of the four spraying modes were validated by using sampled experimental data of droplet charge-to-mass ratio and deposition coverage.

 doi:10.20944/preprints202505.1301.v1

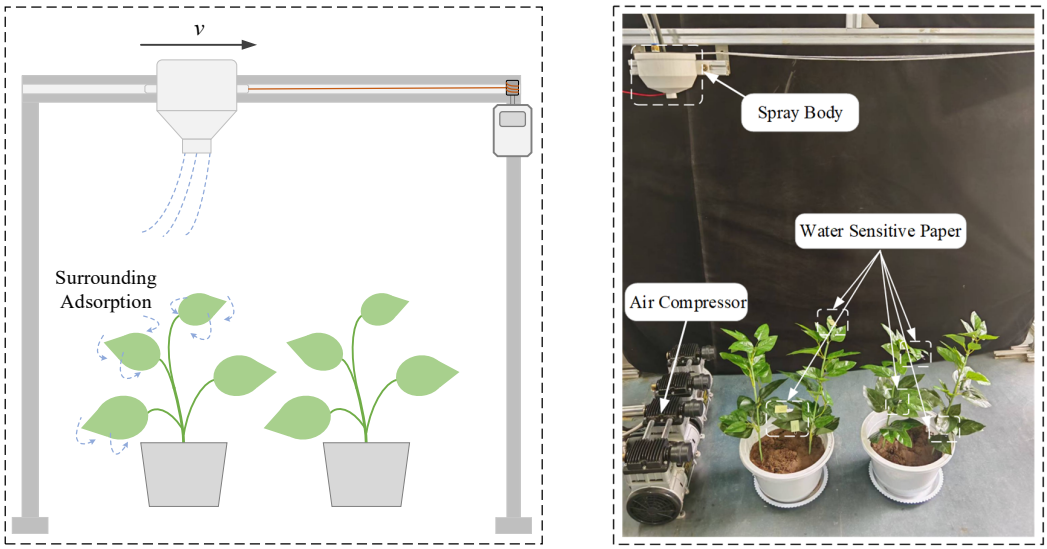

Figure 6. Electrostatic spraying experiment platform: (a) Schematic diagram of the experiment platform; (b) Physical photograph of the experiment platform.

3. Results

3.1. Analysis of Liquid Film Morphology and Breakup Process

During hydraulic atomization, pressurized liquid is delivered from the water tank to the nozzle orifice, forming a hollow cone-shaped liquid film. High-speed imaging observations reveal that the liquid film's geometric dimensions and morphology exhibit significant dynamic variation, as shown in Figure 7. These time-domain features are primarily influenced by airflow disturbances and operational hydraulic pressure.

From a spatial evolution perspective, when the liquid jet reaches a certain distance, the liquid film thickness becomes non-uniform, gradually developing wavelike surface morphology. The liquid film initially ruptures at its thinnest regions, after which the separated liquid fragments undergo further breakup during high-speed motion, ultimately forming fine droplets as illustrated in Figure 8.

Counting the liquid film morphological parameters under multiple sets of steady operating states, the statistical distribution characteristics of liquid film length (L), width (D), and spray angle (α) were obtained. Experimental data indicated that under pure hydraulic atomization conditions, the measured values of liquid film length (L) range from 1.5 to 3.0 mm, width (D) is concentrated in the range of 2.0 - 3.0 mm, and the distribution of spray angle (α) falls between 40° and 70°.

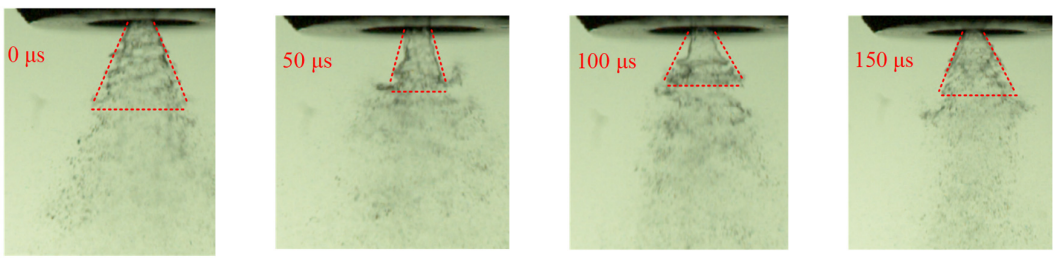

 doi:10.20944/preprints202505.1301.v1

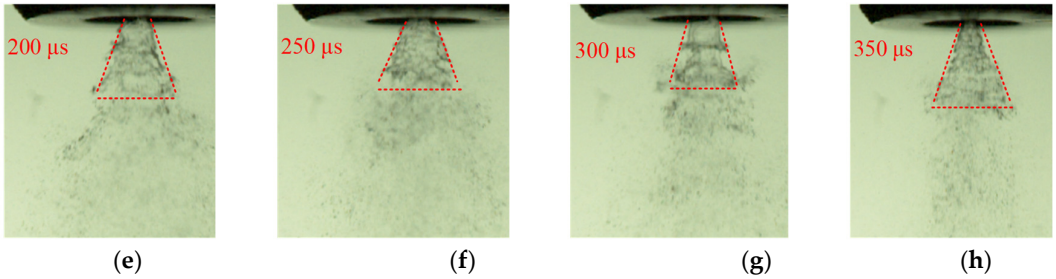

Figure 7. Time-domain development of hollow-cone liquid film.

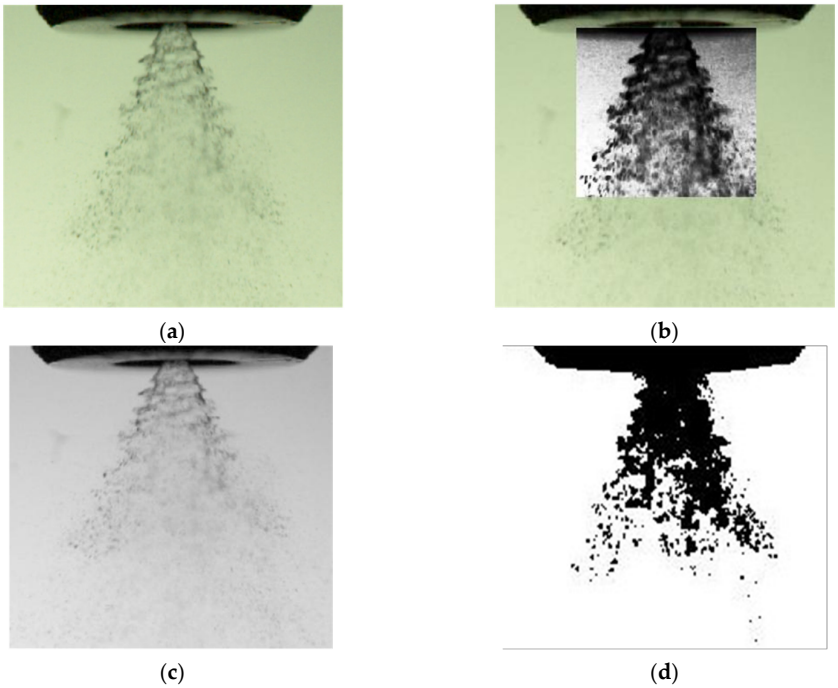

Figure 8. Spatial morphology of hollow-cone liquid film: (a) Original image; (b) Partial grayscale processing; (c) Full grayscale processing; (d) Binarization processing.

Under the hydraulic-pneumatic coupled atomization mode, the introduction of assisted airflow significantly improves the stability of the liquid film, as shown in Figure 9. In this atomization mode, experimental measurements reveal that the liquid film length (L) remains stable within the range of 1.8 - 2.2 mm, the width (D) is maintained between 1.5 - 2.2 mm, and the spray angle (α) distributes within the range of 40° - 60°.

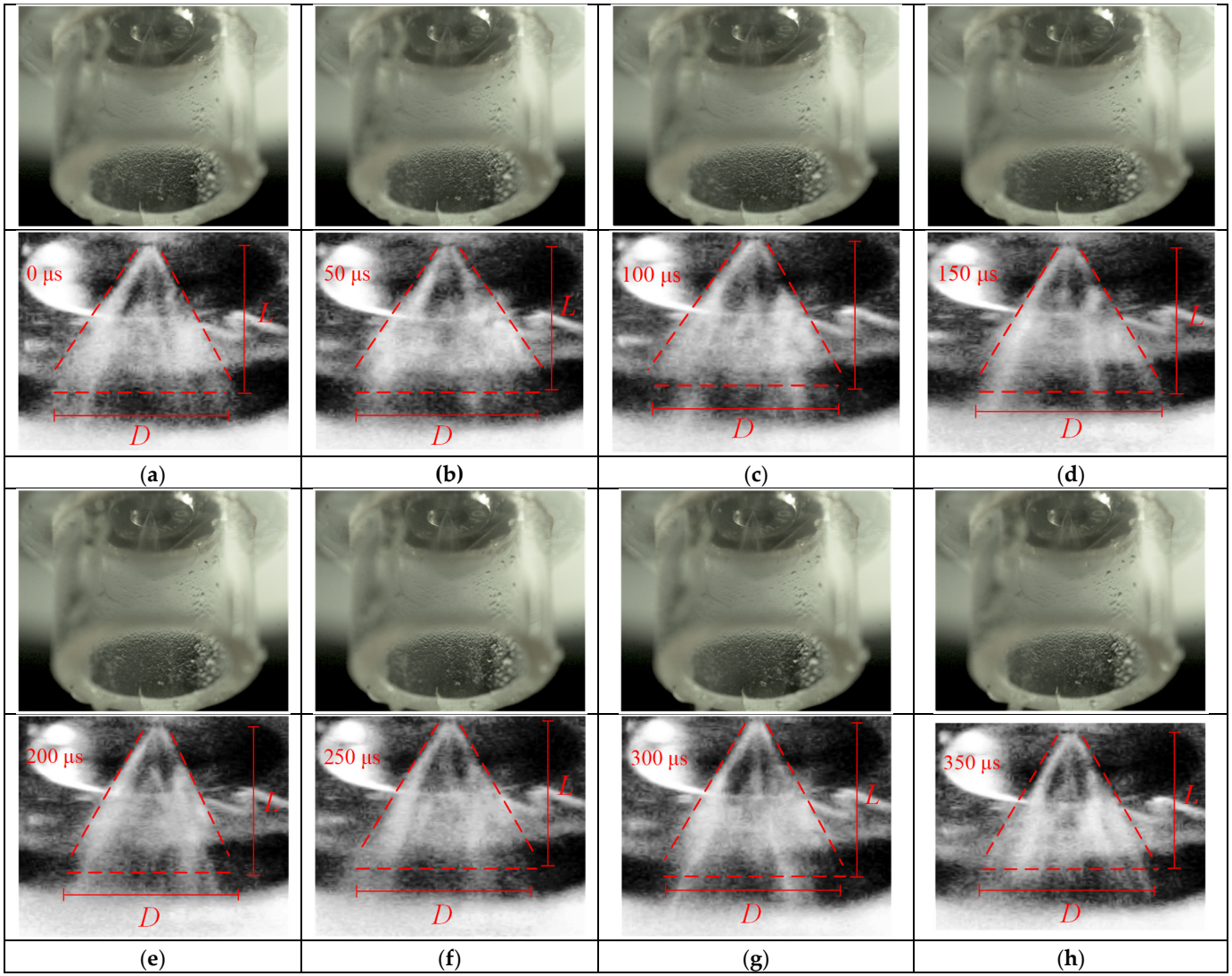

Figure 9. Morphological characteristics of liquid film in hydraulic-pneumatic coupled atomization mode.

 doi:10.20944/preprints202505.1301.v1

As shown in Table 2, compared to the pure hydraulic atomization mode, the morphological parameters of the liquid film under the coupled atomization mode exhibit a significant decreasing trend. This phenomenon arises from two key factors: First, the airflow perpendicular to the liquid film surface generates an inward compression effect, directly leading to a reduction in both the spray angle and the liquid film width. Second, the enhanced airflow disturbance markedly increases the surface instability of the liquid film, promoting earlier-stage breakup and atomization of the liquid film.

Table 2. Morphological parameters of liquid film.

Atomization method	Average liquid film length (L) mm	Average liquid film width (D) mm	Average spray angle (α) °
Hydraulic atomization	2.23	2.51	59.78
Hydraulic-pneumatic atomization	2.14	1.96	49.25

3.2. Analysis of Electric Field Spatial Distribution Based on Finite Element Model

To validate the distortion of liquid films on the spatial electric field, this study first established comparative simulation models to investigate the electric field distribution characteristics with and without the liquid film. The simulation results demonstrate that when the liquid medium reaches an electrostatic equilibrium state, a large number of opposite charges are induced on the outer surface of the conductive liquid film. This phenomenon causes the internal potential of the liquid film to approach zero, while simultaneously changing the overall spatial potential distribution, as illustrated in Figure 10. Comparative analysis reveals that when the distortion effect of the liquid film is not considered, the ring electrode and the metal nozzle tip exhibit distinct electric field intensity extremes, with the maximum field strength at the nozzle tip reaching 2.62×10^6 V/m. However, upon introducing the liquid film, the electric field distribution undergoes significant changes—the extremal point of the electric field strength shift to the leading edge of the liquid film with the value of 3.39×10^6 V/m. Notably, the liquid film only induces significant electric field distortion in its immediate vicinity, while the field distribution in other regions remains largely unaffected.

The presence of the liquid film causes the spatial position and geometric dimensions of the charging electrode to significantly affect both the electric field spatial distribution and the final charging effect. As simulation results shown in Figure 11, the significant ranking of the effect of electrode parameters on droplet charging performance is spatial position, cross-sectional length, cross-sectional width. Specifically, within the studied parameter range, the average surface charge density of the liquid film exhibits a positive correlation with electrode size. When maintaining the electrode dimension parameters as constant, the charge density displays non-monotonic variation with the electrode spatial position: as the electrode moves downward from the top of the charging zone, the charge density initially increases, reaches its maximum when the annular electrode plane coincides with the tangential plane of the liquid film leading edge, and then gradually decreases with further electrode descent. The results indicate that the influence of electrode parameters on liquid film surface charge density is closely related to the morphological characteristics of the liquid film.

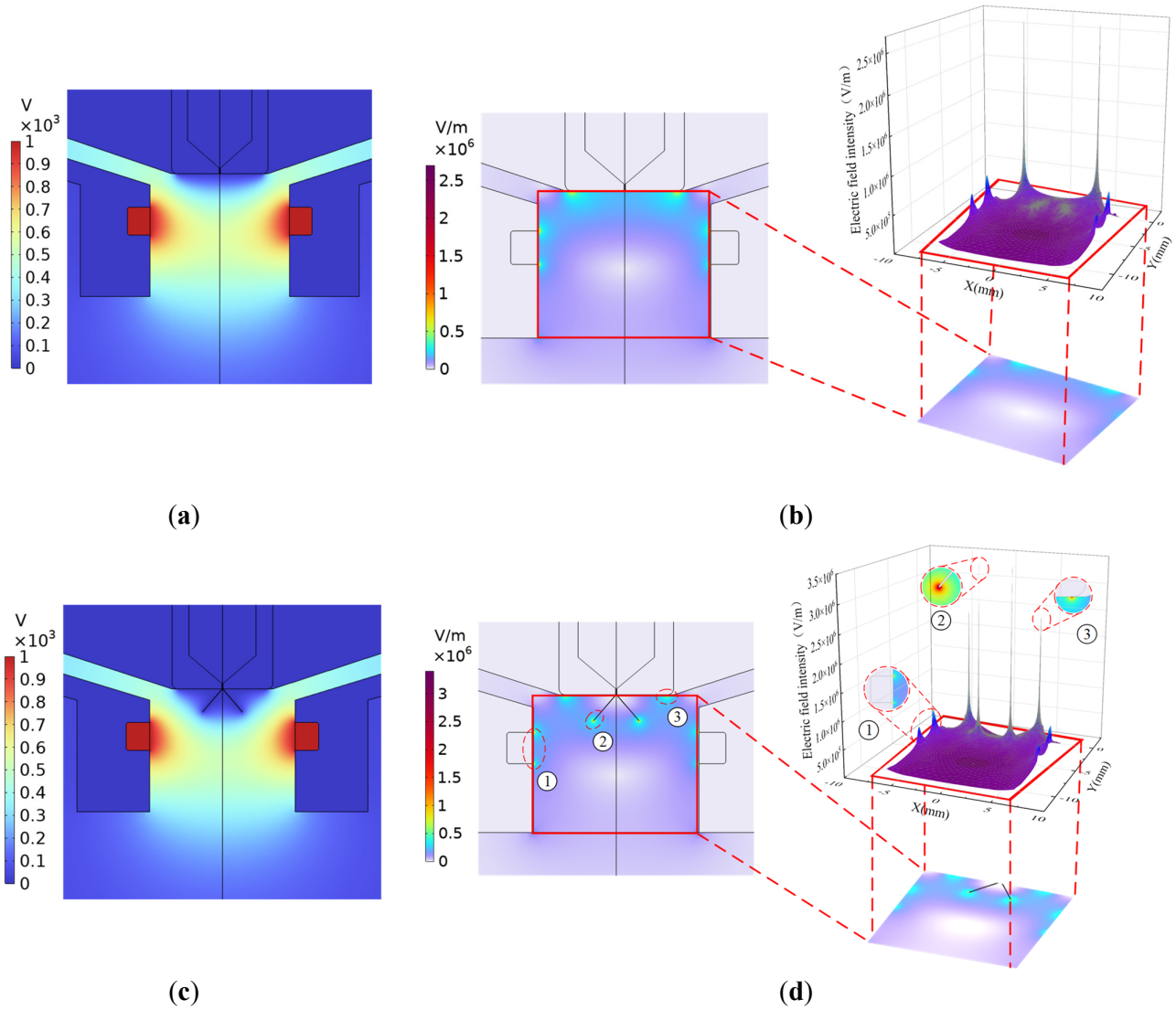

Figure 10. Distortion effect of conductive liquid film on electric field distribution: (a) Potential contour without liquid film; (b) Electric field strength contour without liquid film; (c) Potential contour with liquid film; (d) Electric field strength contour with liquid film.

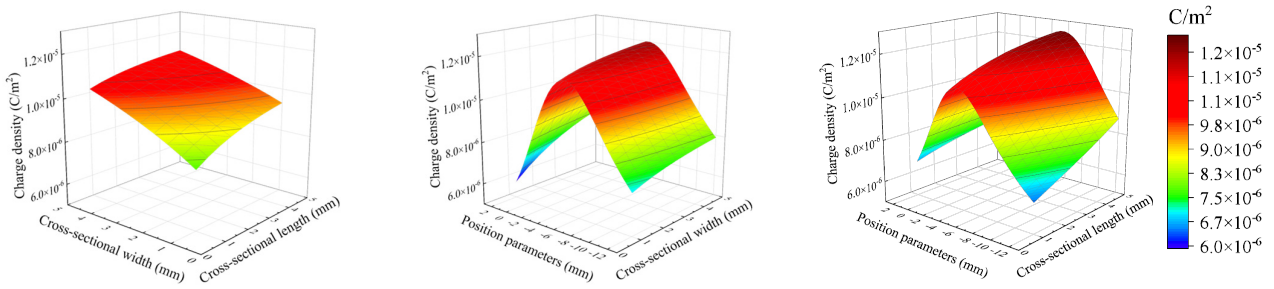

(**a**) (**b**) (**c**)

Figure 11. Influence of electrode parameters on charge density at liquid film leading edge: (a) Effect of electrode cross-section length and width; (b) Effect of electrode position parameter and cross-section width; (c) Effect of electrode position parameter and cross-section length.

 doi:10.20944/preprints202505.1301.v1

3.2. Charging Electrode Optimization for Enhancing Charging Performance

To describe the relationship between charge density and electrode parameters, a BP neural network was employed to establish an agent model. The reliability of the agent model was network performance was comprehensively evaluated using several statistical metrics, including the coefficient of determination (R^2), root mean square error (RMSE), mean absolute error (MAE), and mean bias error (MBE). R^2 reflects the goodness of fit, RMSE characterizes the overall prediction deviation, MAE indicates prediction precision, and MBE evaluates systematic bias characteristics. As shown in Table 3, the training results demonstrate that all evaluating metrics remain at relatively low levels, confirming that the neural network exhibits good reliability and meets the accuracy requirements for charge density prediction.

Table 3. Training performance of the droplet charging agent model.

	R^2	RMSE	MAE	MBE
Training set	0.9994	4.07×10^{-8}	3.12×10^{-8}	-7.67×10^{-12}
Validation set	0.9993	4.03×10^{-8}	2.99×10^{-8}	-1.22×10^{-9}

Based on the established agent model for liquid film surface charge density, this study systematically optimized the electrode parameters. To simplify the computational process, the cross-sectional length l and width d of the electrode were optimized with the equal value in the range of [0, 5] mm. The electrode position parameter y was optimized in the range of [-12, 2] mm. As shown in Table 4, the optimization results indicate that the optimal electrode position automatically adjusts with changes in electrode dimension, consistently maintaining a spatial relationship that the electrode plane coincides with the tangent plane of the liquid film leading edge. It ensures that the liquid film leading edge achieves the maximum charge density. By substituting the optimized parameters into the simulation model, there is a high consistency between predicted values and simulation results, confirming the reliability of this optimization method.

Table 4. Comparison of optimized electrode parameters.

No.	Electrode parameters (l, d, y) (mm)	Predicted value (C/m²)	Simulated value (C/m²)
1	(1, 1, -3.543)	-9.843×10^{-6}	-9.843×10^{-6}
2	(2, 2, -3.825)	-1.115×10^{-5}	-1.118×10^{-5}
3	(3, 3, -4.146)	-1.190×10^{-5}	-1.193×10^{-5}
4	(4, 4, -4.378)	-1.239×10^{-5}	-1.237×10^{-5}
5	(5, 5, -4.984)	-1.258×10^{-5}	-1.263×10^{-5}

The optimizing results demonstrate that appropriately increasing electrode dimensions can indeed enhance the charge induction effect on the liquid film. However, existing studies [28] demonstrate that under actual experimental conditions, excessively large electrode sizes conversely degrade charging performance. This phenomenon can be attributed to the following mechanisms: First, oversized electrodes increase the contact area with the charged atomization zone, promoting the migration and subsequent adhesion of charged droplets to the electrode. Upon adhering on the electrode surface, these droplets are neutralized and subsequently acquire charges of opposite polarity. Second, droplet accumulation on the electrode surface may trigger corona discharge, further deteriorating charging performance.

Therefore, to maintain stable charging performance, electrode dimensions must be confined within a reasonable range. While smaller sizes reduce droplet deposition probability, excessively small electrodes may induce corona discharge due to small edge curvature radius [29]. Based on the measured characteristic length of the liquid film (about 2 mm), this study ultimately adopted a 2 mm×2 mm square electrode. This dimensional design avoids the aforementioned issues while

 doi:10.20944/preprints202505.1301.v1

ensuring effective "wrapping" of the liquid film by the electrode. Under this electrode dimension parameter, the optimal electrode position y was determined as -3.825 mm, as shown in Table 4. Under this configuration, the average charge density at the liquid film leading edge reached 1.12×10^{-5} C/m². Although resulting in an 11.11% reduction in surface average charge density compared to the 5 mm electrode configuration, the 2 mm configuration significantly reduced the droplet deposition probability and elevated the corona inception voltage threshold of the charging atomization zone. Overall, it could achieve better droplet charging performance in actual electrostatic spraying application.

3.4. Comparative Verification of Nozzle Charging Performance

To verify the charging performance of the optimized electrostatic hollow-cone nozzle, this study conducted comparative experiments using a charging electrode with a cross-sectional dimension of 2 mm × 2 mm. The optimal installation position (y = -3.8 mm) was first determined and served as the benchmark. As shown in Figure 12, three test positions (Positions 1, 3, and 4) were sequentially arranged upside and downside the optimal position (Position 2) with the interval of 5 mm. Additionally, to improve the stability of the charging process, all sharp edges of the charging electrodes were chamfered to avoid the corona discharge in the charging atomization zone.

The droplet charging performances under different electrode positions were evaluated through a charge-to-mass ratio measurement platform. As shown in Figure 13, experimental results demonstrate that for three parameter configurations (positions 2, 3, and 4), the droplet charging effect initially strengthens and then weakens with continuous increase of the charging voltage. When the voltage exceeds a critical threshold, the ammeter (15B MAX, Fluke) detects significant leakage current, indicating droplet migration and deposition on the charging electrode, diminishing the droplet charging effect. Notably, the electrode at the optimal position (position 2) exhibits superior performance with the maximum charge-to-mass ratio of 4.9 mC/kg at 3 kV charging voltage. Comparative data reveal that positions 3 and 4 reach 93.7% and 67.9% of the optimal position's maximum charge-to-mass ratio respectively. However, due to charge loss caused by leakage currents, their actual effective charging performance decreases to 77.8% and 61.1% correspondingly. Furthermore, as shown in Figure 12, the charging electrode in position 1 is adjacent to the hollow-cone nozzle. It produced excessive leakage current (>10 μA) even at low voltages, indicating a high susceptibility to corona discharge and significant degradation in droplet charging efficiency.

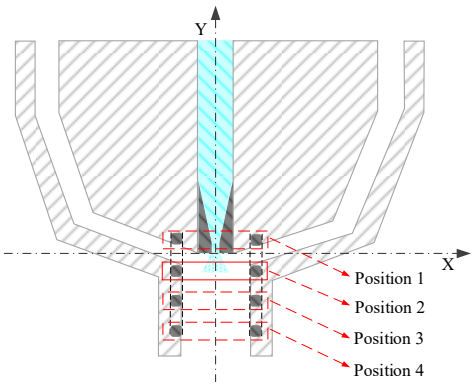

Figure 12. Schematic diagram of electrode placement positions.

 doi:10.20944/preprints202505.1301.v1

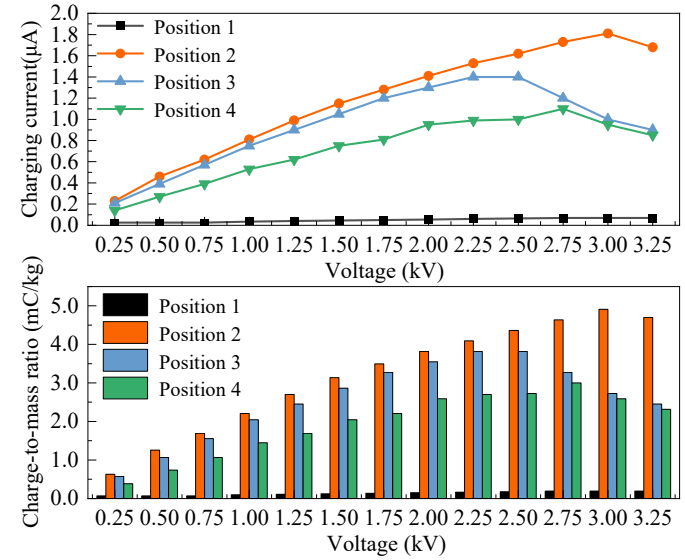

(**a**)

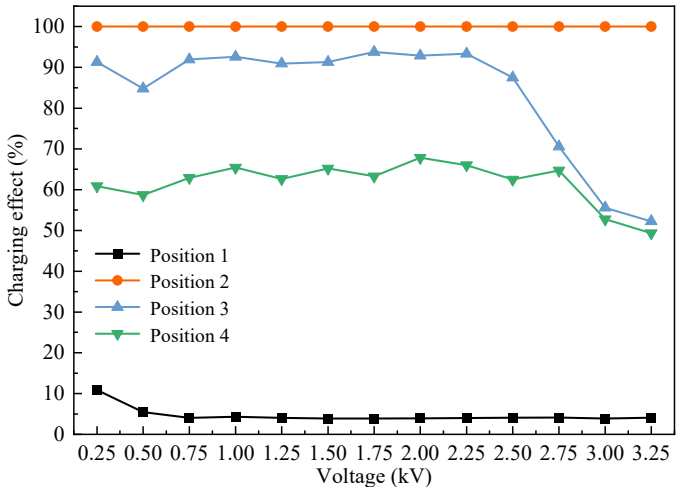

(**b**)

Figure 13. Droplet charging performance under different electrode positions: (a) Charging current and charge-to-mass ratio; (b) Charging efficiency comparison.

To validate the spraying quality of the optimized electrostatic nozzle, this study measured the droplet coverage on soybean leaf using the spraying experiment platform constructed in section 2.5. Four spraying modes, i.e., electrostatic spraying with charging electrode at Position 2, 3, 4 respectively, and non-electrostatic spraying, were adopted in the experiments. In all four modes, the same hollow-cone nozzle was used with the same spraying flowrate of 23 ml/min. And the charging voltage of three electrostatic spraying modes was set as 3.0 kV.

Due to the mutual repulsion of the same-polar charges, the moving charged droplet cloud occupies a larger volume and exhibits a more uniform distribution compared with the uncharged droplets. Consequently, on the adaxial leaf surfaces in the upper soybean canopy, the droplet coverage of electrostatic spraying is slightly lower than that of non-electrostatic spraying. But the droplet deposition uniformity on the leaf surface is significantly improved. On the adaxial leaf surfaces in the middle and lower canopy, the droplet coverage of non-electrostatic spraying decreases substantially compared to electrostatic spraying. On the abaxial leaf surfaces of target canopy, the droplet coverage of non-electrostatic spraying is consistently less than 1%. However, with all three

 doi:10.20944/preprints202505.1301.v1

electrostatic spraying modes, the droplet coverage on the abaxial surfaces increases significantly due to the "wraparound-adsorption" effect.

Specifically speaking, as the charging electrode moves downward from Position 2 to Position 4, the droplet coverages on both the adaxial and abaxial leaf surfaces show a declining trend. When the electrode is at the optimal Position 2, the droplet coverage on the adaxial leaf surfaces of upper, middle and lower canopy layers ranges from 10.71% to 24.31%, while the droplet coverage on the abaxial surfaces reaches 5.72% to 12.19%. Comparatively, when the electrode is at Position 4, the droplet deposition effect becomes worse. The coverage on the adaxial surfaces decreases to 7.72% to 23.55%, and that on the abaxial surfaces decreases to 2.67% to 6.54%. The reason is that the droplet charge-to-mass ratio with the electrode at Position 2 is higher than that at Position 4, so the "wraparound-absorption" effect of charged droplets produced with the electrode at Position 2 is much stronger. Therefore, the droplet deposition effect is highly consistent with the droplet charge-to-mass ratio. The spraying experiment further verified the effectiveness of the optimized electrostatic nozzle.

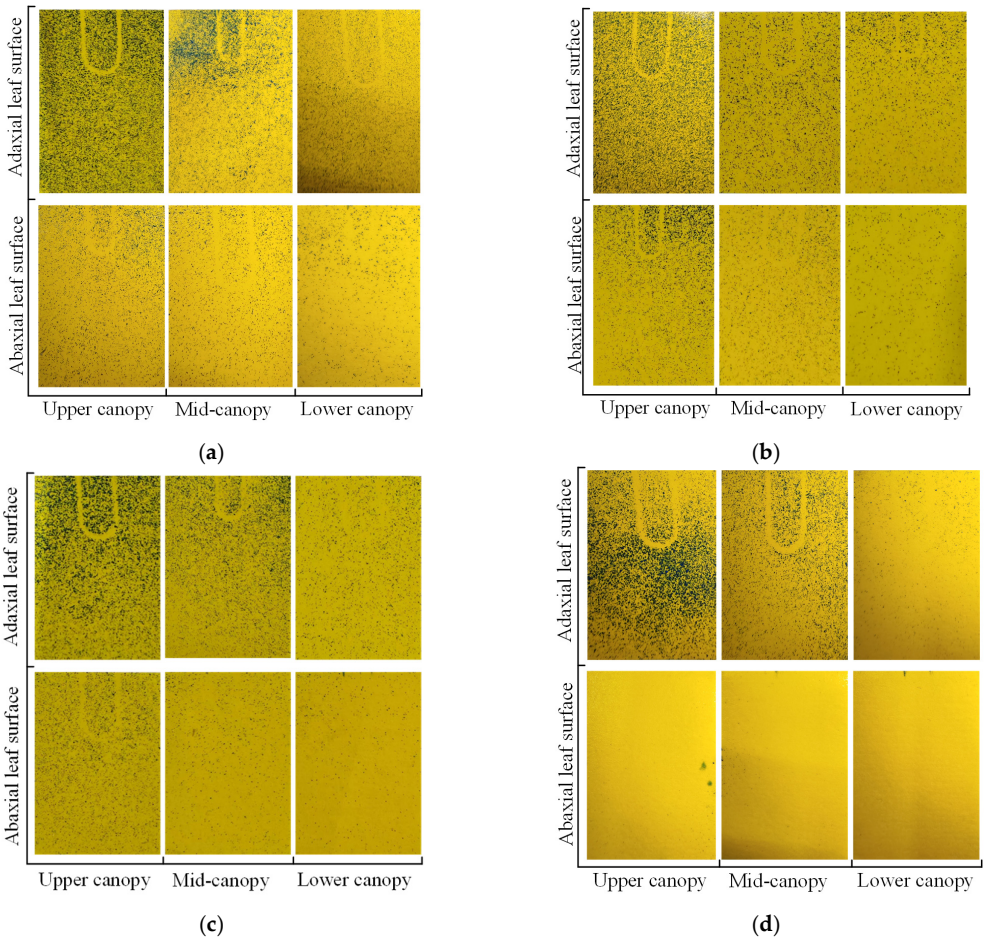

 doi:10.20944/preprints202505.1301.v1

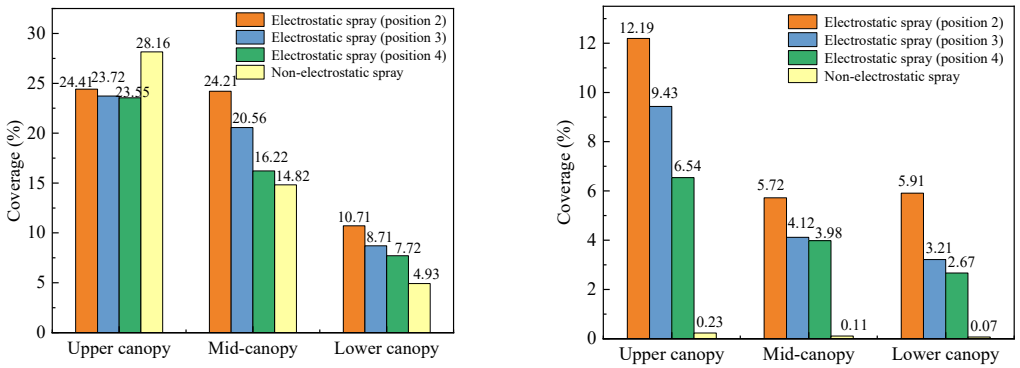

Figure 14. Spraying quality evaluation of the optimized electrostatic nozzle: (a) Droplet deposition with the electrode at Position 2; (b) Droplet deposition with the electrode at Position 3; (c) Droplet deposition with the electrode at Position 4; (d) Droplet deposition with the non-electrostatic spray mode; (e) Droplet coverage of adaxial leaf surfaces; (f) Droplet coverage of abaxial leaf surfaces.

4. Conclusions

Through electrostatic field simulation analysis and electrostatic spraying experiments, this study clarifies design principles for spatial position and dimensional parameters of the charging electrode in the hollow-cone electrostatic nozzle, providing technical support for the broader application of electrostatic spraying technology. The main conclusions are as follows:

(1) Theoretical analysis demonstrates that the presence of a hollow-cone conductive liquid film causes significant distortion to the electric field in the charging atomization zone. The optimal charging performance is achieved when the electrode plane coincides with the tangential plane of the liquid film leading edge. The increase of electrode dimensions theoretically enhances surface charge density but increases the droplet deposition on the electrode and leakage current. So the electrode dimensions should be optimized to approximate the liquid film dimensions.

(2) Based on the optimization rules, with the geometric parameters of the liquid film: length L=2.14 mm, width D=1.96 mm, and spray angle α=49.25°, an annular charging electrode with an inner radius of 6.5 mm, a cross-sectional dimension of 2.0×2.0 mm and a distance of 3.8 mm below the nozzle tip was determined. Compared to unoptimized parameters, the optimized electrostatic nozzle could achieve the best charging effect. Further analysis reveals that the droplet charge-to-mass ratio exhibits nonlinear variation with the increase of charging voltage. The charge-to-mass ratio increases with the voltage in the range of 0-3.0 kV and reaches a peak of 4.9 mC/kg at 3.0 kV. When exceeding 3.0 kV, the charge-to-mass ratio rapidly decreases due to the leakage current induced by droplet deposition on the electrode and corona discharge.

(3) The spraying experiments verified that the optimized electrostatic nozzle could significantly enhance pesticide application effectiveness. Compared with non-electrostatic spraying nozzle and the electrostatic nozzles before parameter optimization, the optimized electrostatic nozzle enhanced droplet coverage on adaxial and abaxial leaf of 10.71%,24.21% and 24.41% and 5.91%, 5.72% and 12.19% respectively. It means that the optimized electrostatic nozzle could achieve more uniform droplet deposition on the whole crop canopy, and obtain better spraying quality and pesticide utilization.

Author Contributions: Conceptualization, L.Z. and X.L.; methodology, X.L.; software, Z.L.; validation, Z.L. and Q.C.; formal analysis, H.C.; investigation, L.Z.; resources, Y.L.; data curation, Q.C.; writing—original draft preparation, Z.L. and H.C.; writing—review and editing, X.L.; visualization, Q.C. and H.C.; supervision, L.Z.; project administration, Y.L.; funding acquisition, Y.L. All authors have read and agreed to the published version of the manuscript.

 doi:10.20944/preprints202505.1301.v1

Funding: This research was funded by Shandong Province Key R&D Plan Project (Major Science and Technology Innovation) (2022LZGC020), National Natural Science Foundation of China (32271992), Natural Science Foundation of Shandong Province (ZR2023MC083).

Data Availability Statement: Dataset available on request from the authors.

Conflicts of Interest: The authors declare no conflicts of interest.

References

1. Guo, J.; Dong, X.; Qiu, B. Analysis of the Factors Affecting the Deposition Coverage of Air-Assisted Electrostatic Spray on Tomato Leaves. *Agronomy* **2024**, *14*, 1108, doi:https://doi.org/10.3390/agronomy14061108.
2. Vigo-Morancho, A.; Videgain, M.; Boné, A.; Vidal, M.; García-Ramos, F.J. Characterization and Evaluation of an Electrostatic Knapsack Sprayer Prototype for Agricultural Crops. *Agronomy* **2024**, *14*, 2343, doi:https://doi.org/10.3390/agronomy14102343.
3. Almekinders, H.; Ozkan, H.E.; Reichard, D.L.; Carpenter, T.G.; Brazee, R.D. Spray Deposit Patterns of an Electrostatic Atomizer. *Transactions of the ASABE* **1992**, *35*, 1361-1367, doi:https://doi.org/10.13031/2013.28741.
4. Wolf, T.M.; Downer, R.; Hall, F.R.; Wagner, O.; Kuhn, P.J. Effect of Electrostatic Charging on the Dose Transfer of Water-Based Pesticide Mixtures. 1996. https://doi.org/10.1520/stp16027s.
5. Salcedo, R.; Sánchez, E.; Zhu, H.; Fàbregas, X.; García-Ruiz, F.; Gil, E. Evaluation of an electrostatic spray charge system implemented in three conventional orchard sprayers used on a commercial apple trees plantation. *Crop Protection* **2023**, *167*, 106212, doi:https://doi.org/10.1016/j.cropro.2023.106212.
6. Wang, S.; Li, X.; Zhou, H.; Lv, X.; Shen, W. Design and Experiment of an Aerial Electrostatic Spraying System for Unmanned Agricultural Aircraft Systems. *Applied Engineering in Agriculture* **2020**, *36*, 955-962, doi:https://doi.org/10.13031/aea.14150.
7. Lin, Z.; Xie, J.; Tian, S.; Wang, X.; Sun, W.; Mo, X. Research and experiment of electrostatic spraying system for agricultural plant protection unmanned vehicle. *Frontiers in Ecology and Evolution* **2023**, *Volume 11 - 2023*, doi:https://doi.org/10.3389/fevo.2023.1138180.
8. Law, S.E. Electrostatic Pesticide Spraying: Concepts and Practice. *IEEE Transactions on Industry Applications* **1983**, *IA-19*, 160-168, doi:https://doi.org/10.1109/TIA.1983.4504176.
9. Patel, M.K.; Kundu, M.; Sahoo, H.K.; Nayak, M.K. Enhanced performance of an air-assisted electrostatic nozzle: Role of electrode material and its dimensional considerations in spray charging. *Engineering in Agriculture, Environment and Food* **2016**, *9*, 332-338, doi:https://doi.org/10.1016/j.eaef.2016.05.002.
10. Mamidi, V.R.; Ghanshyam, C.; Manoj Kumar, P.; Kapur, P. Electrostatic hand pressure knapsack spray system with enhanced performance for small scale farms. *Journal of Electrostatics* **2013**, *71*, 785-790, doi:https://doi.org/10.1016/j.elstat.2013.01.011.
11. Laryea, G.N.; No, S.-Y. Development of electrostatic pressure-swirl nozzle for agricultural applications. *Journal of Electrostatics* **2003**, *57*, 129-142, doi:https://doi.org/10.1016/S0304-3886(02)00122-5.
12. Wang, J.; Zhang, S.; Zuo, Z. Experimental study of influence rules on spray charged characteristics in the induction charging process. *high voltage engineering* **2017**, doi:https://doi.org/10.13336/j.1003-6520.hve.20170123023.
13. Lin, J.; Cai, J.; Ouyang, J.; Xiao, L.; Qiu, B. The Influence of Electrostatic Spraying with Waist-Shaped Charging Devices on the Distribution of Long-Range Air-Assisted Spray in Greenhouses. *Agronomy* **2024**, *14*, 2278, doi:https://doi.org/10.3390/agronomy14102278.
14. Brentjes, A.; Pozarlik, A.K.; Brem, G. Estimating droplet charge in numerical simulations of charged sprays. *Journal of Electrostatics* **2021**, *112*, 103591, doi:https://doi.org/10.1016/j.elstat.2021.103591.
15. Zhao, S.; Castle, G.S.P.; Adamiak, K. The effect of space charge on the performance of an electrostatic induction charging spray nozzle. *Journal of Electrostatics* **2005**, *63*, 261-272, doi:https://doi.org/10.1016/j.elstat.2004.11.001.
16. Kacprzyk, R.; Zylka, P. Electrification of aerosol particles in supersonic atomizers. *IEEE Transactions on Dielectrics and Electrical Insulation* **2011**, *18*, 1353-1360, doi:https://doi.org/10.1109/TDEI.2011.6032802.

 doi:10.20944/preprints202505.1301.v1

17. Vankeswaram, S.K.; Deivandren, S. Size and velocity characteristics of spray droplets in near-region of liquid film breakup in a swirl atomizer. *Experimental Thermal and Fluid Science* **2022**, *130*, 110505, doi:https://doi.org/10.1016/j.expthermflusci.2021.110505.
18. Gañán-Calvo, A.M.; López-Herrera, J.M.; Herrada, M.A.; Ramos, A.; Montanero, J.M. Review on the physics of electrospray: From electrokinetics to the operating conditions of single and coaxial Taylor cone-jets, and AC electrospray. *Journal of Aerosol Science* **2018**, *125*, 32-56, doi:https://doi.org/10.1016/j.jaerosci.2018.05.002.
19. Melcher, J.R.; Taylor, G.I.S. Electrohydrodynamics: A Review of the Role of Interfacial Shear Stresses. *Annual Review of Fluid Mechanics* **1969**, *1*, 111-146, doi:https://doi.org/10.1146/annurev.fl.01.010169.000551.
20. Edward Law, S. Agricultural electrostatic spray application: a review of significant research and development during the 20th century. *Journal of Electrostatics* **2001**, *51-52*, 25-42, doi:https://doi.org/10.1016/S0304-3886(01)00040-7.
21. Belhadef, A.; Vallet, A.; Amielh, M.; Anselmet, F. Pressure-swirl atomization: Modeling and experimental approaches. *International Journal of Multiphase Flow* **2012**, *39*, 13-20, doi:https://doi.org/10.1016/j.ijmultiphaseflow.2011.09.009.
22. Kalitan, D.; Salgues, D.; Mouis, A.; Lee, S.; Pal, S.; Santoro, R. Experimental Liquid Rocket Swirl Coaxial Injector Study Using Non-Intrusive Optical Techniques. In *41st AIAA/ASME/SAE/ASEE Joint Propulsion Conference & Exhibit*.
23. Cejpek, O.; Maly, M.; Prinz, F.; Hajek, O.; Jedelsky, J.; Jicha, M. Adaptation of conical liquid sheet and spray morphologies to cross-flowing gas. *International Journal of Multiphase Flow* **2024**, *172*, 104714, doi:https://doi.org/10.1016/j.ijmultiphaseflow.2023.104714.
24. Makhnenko, I.; Alonzi, E.R.; Fredericks, S.A.; Colby, C.M.; Dutcher, C.S. A review of liquid sheet breakup: Perspectives from agricultural sprays. *Journal of Aerosol Science* **2021**, *157*, 105805, doi:https://doi.org/10.1016/j.jaerosci.2021.105805.
25. Zhang, M.; Xiao, M.; Han, F.; Jiang, L.; Li, C.; Wang, P.; Liao, Y.; Pan, Y. Effects of electric field on Rayleigh limit of nanoscale water droplets: molecular dynamics simulation. *Journal of Physics D: Applied Physics* **2023**, *56*, 025203, doi:https://doi.org/10.1088/1361-6463/aca3b5.
26. Law, S.E. Embedded- Electrode Electrostatic-Induction Spray-Charging Nozzle: Theoretical and Engineering Design. *Transactions of the ASAE* **1978**, *21*, 1096-1104, doi:https://doi.org/10.13031/2013.35448.
27. Post, S.L.; Roten, R.L. A Review of the Effects of Droplet Size and Flow Rate on the Chargeability of Spray Droplets in Electrostatic Agricultural Sprays. *Transactions of the ASABE* **2018**, *61*, 1243-1248, doi:https://doi.org/10.13031/trans.12516.
28. Hensley, J.L.; Feng, X.; Bryan, J.E. Induction charging nozzle for flat fan sprays. *Journal of Electrostatics* **2008**, *66*, 300-311, doi:https://doi.org/10.1016/j.elstat.2007.08.012.
29. Law, S.E.; Lane, M.D. Electrostatic Deposition of Pesticide Sprays onto Ionizing Targets: Charge- and Mass-Transfer Analysis. *IEEE Transactions on Industry Applications* **1982**, *IA-18*, 673-679, doi:https://doi.org/10.1109/TIA.1982.4504125.